

Fabrication and characterization of polyimide-based 'smooth' titanium nitride microelectrode arrays for neural stimulation and recording

Rodrigues, F.; Ribeiro, J.F.; Anacleto, P.A.; Fouchard, A.; David, O.; Sarro, P.M.; Mendez, P.M.

DOI

[10.1088/1741-2552/ab4dbb](https://doi.org/10.1088/1741-2552/ab4dbb)

Publication date

2019

Document Version

Final published version

Published in

Journal of Neural Engineering

Citation (APA)

Rodrigues, F., Ribeiro, J. F., Anacleto, P. A., Fouchard, A., David, O., Sarro, P. M., & Mendez, P. M. (2019). Fabrication and characterization of polyimide-based 'smooth' titanium nitride microelectrode arrays for neural stimulation and recording. *Journal of Neural Engineering*, 17 (2020)(1), 1-15. Article 016010. <https://doi.org/10.1088/1741-2552/ab4dbb>

Important note

To cite this publication, please use the final published version (if applicable). Please check the document version above.

Copyright

Other than for strictly personal use, it is not permitted to download, forward or distribute the text or part of it, without the consent of the author(s) and/or copyright holder(s), unless the work is under an open content license such as Creative Commons.

Takedown policy

Please contact us and provide details if you believe this document breaches copyrights. We will remove access to the work immediately and investigate your claim.

Green Open Access added to TU Delft Institutional Repository

'You share, we take care!' - Taverne project

<https://www.openaccess.nl/en/you-share-we-take-care>

Otherwise as indicated in the copyright section: the publisher is the copyright holder of this work and the author uses the Dutch legislation to make this work public.

PAPER

Fabrication and characterization of polyimide-based 'smooth' titanium nitride microelectrode arrays for neural stimulation and recording

To cite this article: F Rodrigues *et al* 2020 *J. Neural Eng.* **17** 016010

View the [article online](#) for updates and enhancements.

Recent citations

- [A Polyimide-Based Flexible Monopole Antenna Fed by a Coplanar Waveguide](#)
Dingyong Cang *et al*



PAPER

Fabrication and characterization of polyimide-based ‘smooth’ titanium nitride microelectrode arrays for neural stimulation and recording

RECEIVED
18 March 2019REVISED
4 October 2019ACCEPTED FOR PUBLICATION
15 October 2019PUBLISHED
13 December 2019F Rodrigues^{1,3,4}, J F Ribeiro¹, P A Anacleto¹, A Fouchard², O David², P M Sarro³ and P M Mendes¹¹ CMEMS-UMinho, University of Minho, Braga, Portugal² Grenoble Institute of Neurosciences, Grenoble, France³ Electronics Components, Technology, and Materials Lab, Else Kooi Laboratory, Delft University of Technology, Delft, The Netherlands⁴ Author to whom any correspondence should be addressed.E-mail: fabior.2010@gmail.com**Keywords:** peripheral nerve interfaces, nerve cuff electrodes, die-compatible process, titanium nitride electrode, polyimide composite electrodes, sub-millimeter nervesSupplementary material for this article is available [online](#)**Abstract**

Objective. As electrodes are required to interact with sub-millimeter neural structures, innovative microfabrication processes are required to enable fabrication of microdevices involved in such stimulation and/or recording. This requires the development of highly integrated and miniaturized systems, comprising die-integration-compatible technology and flexible microelectrodes. To elicit selective stimulation and recordings of sub-neural structures, such microfabrication process flow can benefit from the integration of titanium nitride (TiN) microelectrodes onto a polyimide substrate. Finally, assembling onto cuffs is required, as well as electrode characterization. *Approach.* Flexible TiN microelectrode array integration and miniaturization was achieved through microfabrication technology based on microelectromechanical systems (MEMS) and complementary metal-oxide semiconductor processing techniques and materials. They are highly reproducible processes, granting extreme control over the feature size and shape, as well as enabling the integration of on-chip electronics. This design is intended to enhance the integration of future electronic modules, with high gains on device miniaturization. *Main results.* (a) Fabrication of two electrode designs, (1) 2 mm long array with 14 TiN square-shaped microelectrodes ($80 \times 80 \mu\text{m}^2$), and (2) an electrode array with $2 \text{ mm} \times 80 \mu\text{m}$ contacts. The average impedances at 1 kHz were 59 and $5.5 \text{ k}\Omega$, respectively, for the smaller and larger contacts. Both designs were patterned on a flexible substrate and directly interconnected with a silicon chip. (b) Integration of flexible microelectrode array onto a cuff electrode designed for acute stimulation of the sub-millimeter nerves. (c) The TiN electrodes exhibited capacitive charge transfer, a water window of -0.6 V to 0.8 V , and a maximum charge injection capacity of $154 \pm 16 \mu\text{C cm}^{-2}$. *Significance.* We present the concept, fabrication and characterization of composite and flexible cuff electrodes, compatible with post-processing and MEMS packaging technologies, which allow for compact integration with control, readout and RF electronics. The fabricated TiN microelectrodes were electrochemically characterized and exhibited a comparable performance to other state-of-the-art electrodes for neural stimulation and recording. Therefore, the presented TiN-on-polyimide microelectrodes, released from silicon wafers, are a promising solution for neural interfaces targeted at sub-millimeter nerves, which may benefit from future upgrades with die-electronic modules.

1. Introduction

Implantable microelectrode arrays (MEAs) based on microfabrication methods continue to evolve,

and possible applications continue to grow in both the central and peripheral nervous systems [1]. Advances in microfabrication methods enable the manufacturing of heterogeneous arrays for distinct

neural structures with improved functionalities. The Utah electrode arrays, based on silicon, first introduced as recording units for the cortex [2], were later modified and used for peripheral nerve applications [3, 4]. The micromachining of polyimide, initially employed in the manufacturing of cuff electrodes for the sciatic nerve [5], has expanded tremendously and is now used in devices for cortical microstimulation and sensing [6] and opto-electric devices [7]. Polyimides have, indeed, been used as support materials in many flexible MEAs in combination with different electrode materials: platinum [8], sputtered iridium oxide (SIROF) [9], graphene [6] and carbon fibers [10]. The present work introduces a microfabrication method which combines polyimide with sputtered titanium nitride (TiN) as electrodes. Two advantages of using TiN as the electrode material in neural implants are (1) its capacitive charge transfer with no irreversible reactions at low charge injection limits [11], and (2) because it is widely used in complementary metal-oxide semiconductor (CMOS) circuitries [12]. By taking advantage of the use of TiN in the CMOS industry [13], integrated neural implants can be designed with local signal conditioning, wireless communication and other electrical modalities.

TiN was first introduced as a sensing and stimulation material by Janders *et al* with a large charge injection capacity (Q_{inj}) of 23 mC cm^{-2} being reported [14]. In their work, rigid electrodes composed of 900 nm thick TiN films on silicon nitride layers were obtained by physical vapor deposition (PVD) sputtering in an argon/nitrogen (50/50) environment. Since the electrochemistry of sputtered TiN electrodes is highly dependent on processing parameters like nitrogen pressure [15, 16] and the underlying layers [17], particular care is advised when comparing the Q_{inj} of TiN electrodes across different works. For example, increasing the nitrogen pressure in the deposition chamber increases the N/Ti atomic ratio in TiN films, leading to significant changes in its voltammetry. For N-rich TiN films, voltammograms shift from a capacitive behavior at low sweep rates (below 100 mV s^{-1}) to a resistive or Ohmic-like behavior at higher sweep rates (above 100 mV s^{-1}), a characteristic of porous electrodes [16, 18]. On the contrary, in smoother, Ti-rich TiN films the charge injection mechanism is predominantly capacitive independently of sweep rates. Likewise, wide variation in the active surface areas of electrodes across different works hampers comparison of their electrochemical properties. Works on TiN microelectrodes have reported a Q_{inj} of 23 mC cm^{-2} [14] and $550/950 \text{ } \mu\text{C cm}^{-2}$ [19], respectively, for areas of $83 \text{ } \mu\text{m}^2$ and $4000 \text{ } \mu\text{m}^2$, while a much lower Q_{inj} of $24 \text{ } \mu\text{C cm}^{-2}$ was reported on TiN macroelectrodes with an area of 6 mm^2 [20]. These previous results on TiN electrodes suggest an inverse correlation between area and charge injection, similarly to that reported for SIROF electrodes [9].

Multipolar cuffs are one type of peripheral nerve electrode that encompass MEAs and use steering

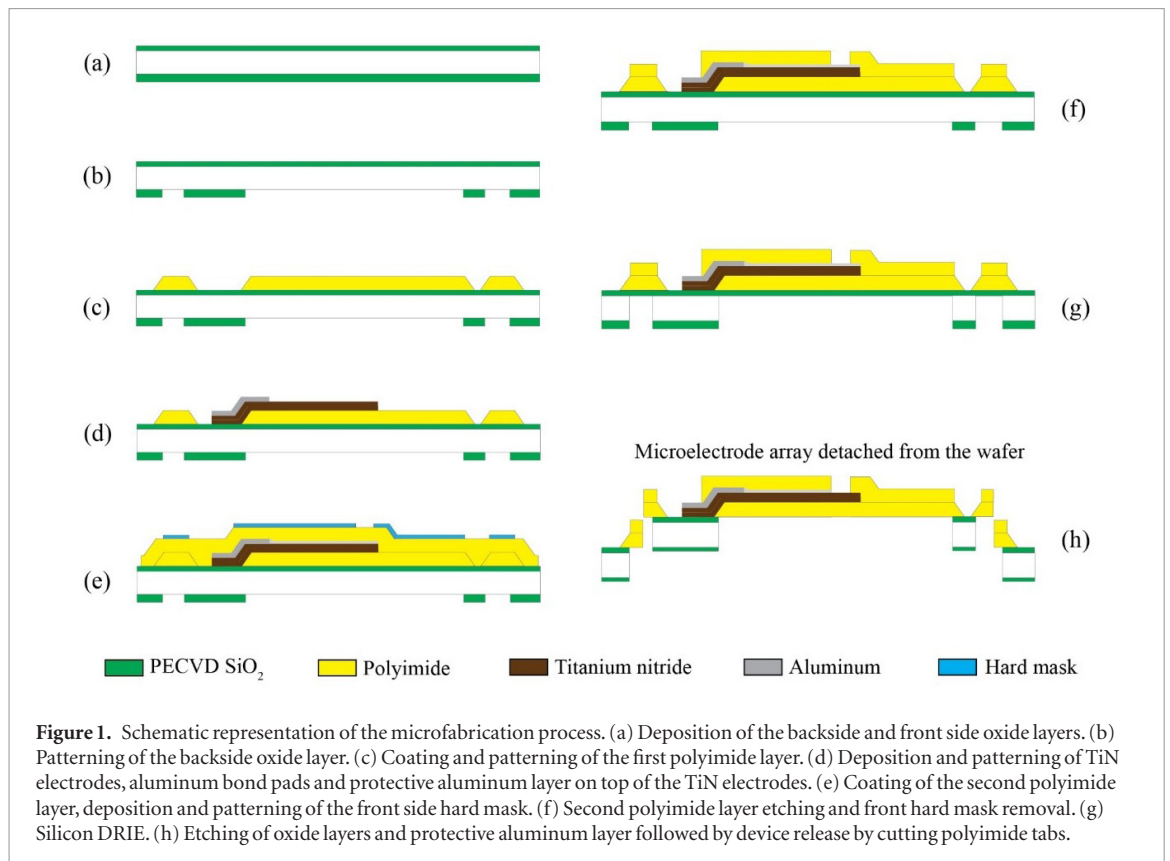
currents across transversal contacts (placed around the nerve) to enable selective stimulation of fascicles within nerve bundles [21, 22]. Flexible cuff MEAs with small diameters ($<1 \text{ mm}$) and a high number of transversal contacts have been fabricated by microfabrication and microelectromechanical systems (MEMS) technologies for peripheral nerve stimulation [23, 24], recording [25] and regeneration [26]. Applications requiring sub-millimeter cuffs with increased density of contacts keep growing fast and are very diverse, ranging from research in small animal nerves [27] to restoration of upper limb movement in humans [28] and electrical impedance tomography [29].

Here, we describe a microfabrication method for fabricating TiN MEAs with small interconnects, addressing the requirements of the high density of contacts listed above. Although inspired by other methods to integrate microelectrodes on polyimide substrates, such as the work of Myllymaa *et al* on polyimide-titanium-platinum devices [30] and the work of Tolstosheeva *et al* on polyimide-titanium-gold [31], our approach adds an electrode material which is widely used in CMOS industries, and does so by employing low-temperature processes only ($<400 \text{ }^\circ\text{C}$), making it compatible with the back-end process. In this way it is possible to achieve seamless integration of electronic, optics, sensor modules and antennas. It is possible to manufacture MEAs of arbitrary shape, enabling the microfabrication method to be customized to different anatomical or neural requirements. High-density TiN MEAs with $6400 \text{ } \mu\text{m}^2$ contacts were mounted on split-cylinder cuffs, thus unveiling ready-to-use and self-closing structures, targeted at sub-millimeter nerves. The advantages of mounting the polyimide-based microelectrodes on cuffs are the ease of handling and surgical placing because, when handled alone, thin films of polyimide tend to curl in undesirable and unpredictable ways and to adhere to non-target structures. The customizability of the microfabrication process is demonstrated by realizing electrodes with a larger area of $160000 \text{ } \mu\text{m}^2$, suitable for cortical applications [31]. Electrochemical testing of TiN microelectrodes (with contact area of $6400 \text{ } \mu\text{m}^2$) on polyimide demonstrated a capacitive charge injection and charge injection capacity of $154 \pm 16 \text{ } \mu\text{C cm}^{-2}$.

2. Methods

2.1. On-wafer microfabrication method

100 mm diameter, $525 \text{ } \mu\text{m}$ thick, single-side-polished silicon wafers were used as the substrate. Figure 1 shows a schematic of the microfabrication steps. A $6 \text{ } \mu\text{m}$ thick silicon dioxide (SiO_2) layer was deposited on the back of a silicon wafer using plasma-enhanced chemical vapor deposition (PECVD). Then, a $1 \text{ } \mu\text{m}$ SiO_2 layer was deposited, also by PECVD, on the front side (figure 1(a)). The $6 \text{ } \mu\text{m}$ SiO_2 backside layer was patterned using $3 \text{ } \mu\text{m}$ thick photoresist as a masking layer for plasma etching. The etching of SiO_2



was done with a plasma containing CF_4 (50 sccm), CHF_3 (25 sccm) and He (40 sccm). The backside SiO_2 will be used as a hard-etch mask during a deep reactive ion etching (DRIE) step at a later stage of the process (figure 1(b)). A $16 \mu\text{m}$ polyimide (PI2611, HD MicroSystems) base layer was spin-coated on the front side. This layer was soft-baked for 7 min on a hot plate at 140°C , followed by a 2 h curing at 400°C in a low-pressure nitrogen environment. After curing, a $10 \mu\text{m}$ thick polyimide layer was achieved, and its thickness was measured with a profilometer and scanning electron microscope (SEM). Subsequently, a 200 nm thick tetraethylorthosilicate oxide (TEOS) layer was deposited by PECVD at 300°C . Then this layer was patterned, using $2 \mu\text{m}$ thick photoresist as a masking layer combined with plasma etching. The PECVD TEOS will later be used as a hard mask during the polyimide dry etching. A two-step approach was followed regarding the polyimide dry etching. First, a pure oxygen plasma was used to etch the first $6 \mu\text{m}$ of polyimide (etch rate: $2\text{--}5 \mu\text{m min}^{-1}$). The polyimide etching was concluded using a plasma with 80% O_2 , 13% N_2 and 7% CF_4 in order to remove any silicon residue [32]. Then, the TEOS mask layer was removed by wet etching using buffered hydrofluoric acid 7:1 (figure 1(c)). After the polyimide etching and patterning, a stack of three metals was sputtered at 300°C without breaking the vacuum: a 40 nm thick titanium layer as an adhesion layer on the polyimide, followed by 200 nm thick TiN as the electrode material, and $2.5 \mu\text{m}$ aluminum, used to form bond pads on the silicon chip. Aluminum was chosen to form the bond

pads instead of TiN because of its better mechanical properties like hardness; additionally, as the bonding wires are also made of aluminum, this leads to the best electrical connection between the pads and wires. The patterning of the aluminum layer was done by thinning it down from $2.5 \mu\text{m}$ to $250\text{--}300 \text{ nm}$ using a $1.4 \mu\text{m}$ thick photoresist layer as a mask and a chlorine-based plasma. After that, wet etching with a PES-type etchant was used to remove the remaining aluminum.

This approach guaranteed that the TiN layer was not etched by the chlorine-based plasma. A $2.5 \mu\text{m}$ thick aluminum is used for bond pads and to achieve a good step coverage in interconnects between the silicon dies and the polyimide layer. A second, 100 nm thick aluminum layer was then sputtered at 25°C . This layer is used for protection of the TiN surface in subsequent steps like dry etching of the second polyimide layer. TiN and the 100 nm thick aluminum were then patterned using chlorine-based plasma (figure 1(d)). A second polyimide layer was spin-coated, soft-baked and cured following the same procedure described for the first layer. After curing of the second polyimide layer, a 200 nm thick TEOS layer was deposited by PECVD on top, and used as a hard mask layer for the polyimide dry-etching step (figure 1(e)). Etching of TEOS was done with the same plasma used for the backside $6 \mu\text{m}$ SiO_2 . Polyimide anisotropic dry etching was performed to define polyimide layout, i.e. electrode contacts, bond pads, holes and tabs (figure 1(f)). The wafer backside processing consisted of anisotropic silicon etching by DRIE using the Bosch process, plus dry etching of the $1 \mu\text{m}$ thick SiO_2 used as an etch-

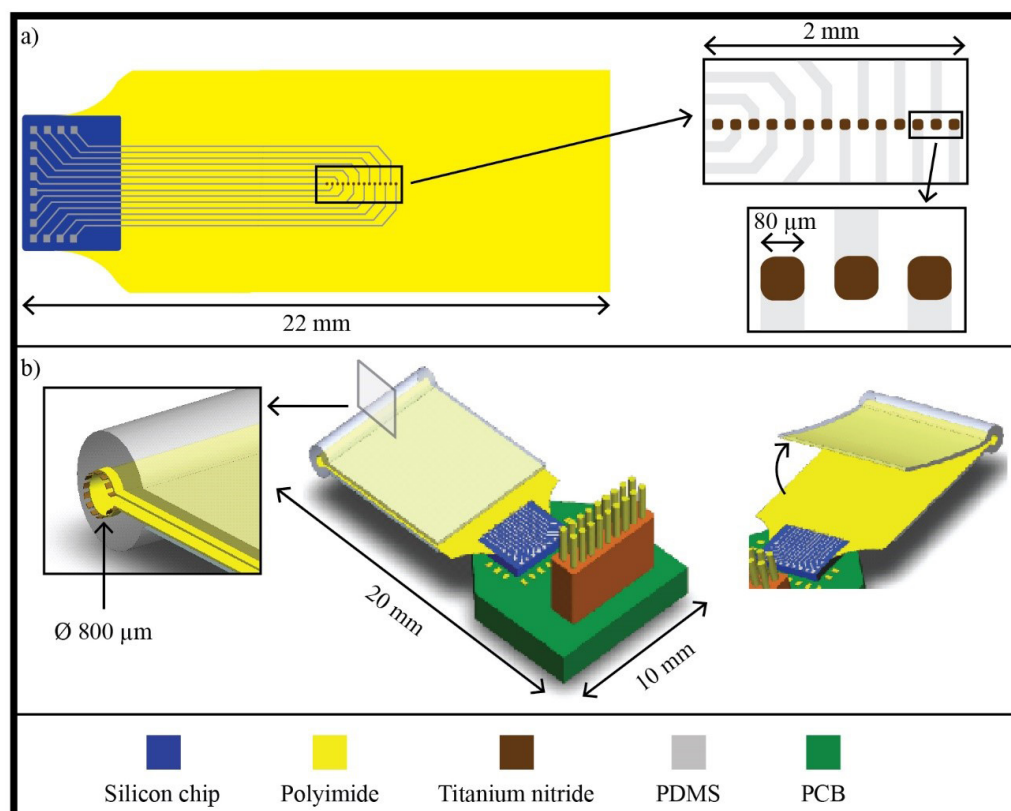


Figure 2. Schematic representation of the split-cylinder cuff with TiN MEA, customized PCB and connector. (a) The flexible polyimide shank attached to a silicon chip and close-up view of the 14 TiN contacts for stimulation. The length of the 14-contact array is 2 mm, and each contact measures $80\ \mu\text{m} \times 80\ \mu\text{m}$. (b) Polyimide-on-PDMS cuff system with the 14 contacts distributed inside the $\text{Ø } 800\ \mu\text{m}$ cuff. The split-cylinder cuff opens for nerve insertion and a connector forms the interface with the outside.

stop layer in the DRIE (figure 1(g)). Finally, etching of the protective $100\ \mu\text{m}$ thick aluminum layer on top of the TiN contacts was performed using a timed wet-etching step with a PES-type etchant (selective to TiN). The entire electrode system remained attached to the wafer by polyimide tabs that could be easily cut with any cutting instrument to mechanically remove the device (figure 1(h)). In addition to the silicon dies with bond pads, bare silicon dies were patterned on the opposite extremity of the device. These prevented the polyimide foils from curling, and facilitated assembly on the cuff.

2.2. DC magnetron sputtering of TiN

TiN was deposited by direct current (DC) magnetron sputtering, using a titanium target of 332 mm diameter with 99.999% purity, and using a Sigma 204 SPTS deposition system. The distance between the target and silicon wafer was 27.5 mm, at a base pressure of 1.33×10^{-7} mbar. During deposition the silicon wafer was flat. At this pressure the chamber was purged with pure argon (20 sccm) and nitrogen (70 sccm). The working pressure during the deposition of titanium and TiN ranged between 0.007 and 0.013 mbar. The sputtering of 40 nm thick titanium was done in 30 s, and the sputtering of 200 nm thick TiN was done in 10 min, both at a target power of 6 kW.

2.3. Device design

A cuff MEA with 14 TiN electrodes distributed over a 2 mm length was designed as shown in figure 2. Each electrode has an $80\ \mu\text{m} \times 80\ \mu\text{m}$ area and the interconnects are $80\ \mu\text{m}$ wide. The area of the polyimide foil supporting the contacts is $20\ \text{mm} \times 6\ \text{mm}$. The holes are patterned in polyimide layers to allow mounting of foil onto the pre-molded cuff (holes are not shown in the schematics of figure 2, but can be seen in the fabricated devices in figure 3). A rigid silicon die ($2.5\ \text{mm} \times 3.8\ \text{mm}$) with bond pads is also defined during the lithography stage of the microfabrication process, as shown in figure 2(a). This will be used to interface the MEA with a printed circuit board (PCB), as shown in figure 2(b). After detaching the MEA from the wafer, the silicon die is glued to a customized PCB, and the bond pads are wire-bonded. An 18-pin connector (Omnetics Connector Corporation, Minneapolis, USA) is welded on the PCB. Bonding wires are protected with a non-conductive glue or polydimethylsiloxane (PDMS) to avoid breakages during cuff assembly. A microfabrication process that yields a hybrid structure with rigid silicon dies connected to flexible polyimide foils has been preferred over others that would otherwise lead to fully flexible devices with polyimide only. The motivations are that in a hybrid structure it

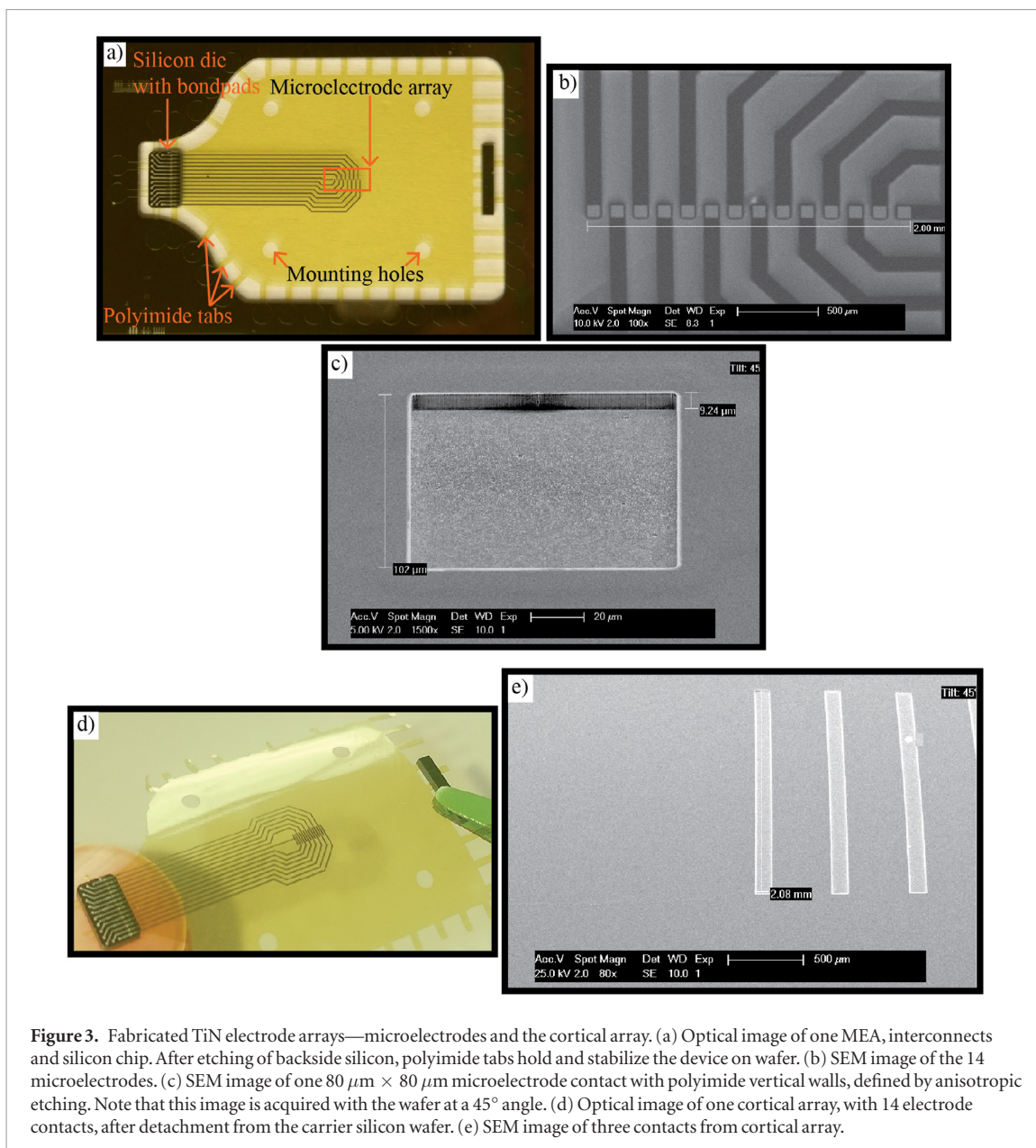


Figure 3. Fabricated TiN electrode arrays—microelectrodes and the cortical array. (a) Optical image of one MEA, interconnects and silicon chip. After etching of backside silicon, polyimide tabs hold and stabilize the device on wafer. (b) SEM image of the 14 microelectrodes. (c) SEM image of one $80\ \mu\text{m} \times 80\ \mu\text{m}$ microelectrode contact with polyimide vertical walls, defined by anisotropic etching. Note that this image is acquired with the wafer at a 45° angle. (d) Optical image of one cortical array, with 14 electrode contacts, after detachment from the carrier silicon wafer. (e) SEM image of three contacts from cortical array.

is possible to integrate active electronic components for signal conditioning and other electronic modules. Additionally, wire bonding on bond pads in rigid structures is a straightforward process, but not when done on flexible structures like polyimide.

In order to demonstrate the customizability of the microfabrication process, a second electrode design with electrode contacts of $2\ \text{mm} \times 80\ \mu\text{m}$ was processed, following the steps described in section 2.1. This second electrode design with larger area is thereby referred to as a cortical array, because the larger area of its contacts makes it suitable for cortical applications. Like the MEA with $80\ \mu\text{m} \times 80\ \mu\text{m}$ electrode contacts, the polyimide-based cortical array interfaces with a rigid silicon die for external routing.

2.4. Cuff assembly

The polyimide-based MEA was transferred to a pre-molded, split-cylinder cuff structure with $800\ \mu\text{m}$ inner diameter as shown in figure 2(b). For molding cuffs, a die-casting structure was developed for PDMS molding, and a mounting tool with alignment pins for cuff device assemblage. A description of the molding and assembly processes can be found in a previous publication [33]. The polyimide and PDMS are glued together using the silicone adhesive MED-2000 (NuSil Technology LLC, California, USA). The positioning and alignment of these two structures was done by matching the mounting holes in the polyimide with those of the customized mounting tool. Once fixed, the flexible polyimide conforms to the molded PDMS,

curling over itself, thus creating a tubular section for the nerve to be inserted in, and making the electrodes radially symmetrical. Cuff repositioning during *in vivo* experiments is possible by simply opening the cuff, as shown in figure 2(b).

2.5. *In vitro* characterization of electrodes

2.5.1. Electrochemical impedance spectroscopy

Electrochemical impedance spectroscopy (EIS) was performed using a Gamry Reference 600 potentiostat combined with the Gamry Framework™. A three-electrode configuration was employed using a large-area (40 mm × 40 mm) platinum counter electrode, an Ag|AgCl (saturated KCl) reference electrode and 28 TiN microelectrodes (80 μm × 80 μm) from two different wafers as the working electrodes. Ten contacts of the cortical array with 2 mm × 80 μm contacts were also analyzed. All potentials are reported with respect to the Ag|AgCl reference electrode. The electrolyte employed was phosphate-buffered saline (PBS, 1X, ρ = 62 Ω•cm) at pH 7.4. The impedance spectra were characterized between 1 Hz and 1 MHz in an open circuit applying an AC signal equal to a 10 mV rms sine wave. Measurements were done at room temperature and after the open circuit potential was at equilibrium. Also, the lumped parameters of an equivalent circuit were fitted with EC-Lab software, using a constant phase angle impedance element (CPE) shunted by a polarization resistance (R_p), in series with the electrolyte resistance (R_e) [34]. The CPE is given by equation (1):

$$Z_{\text{CPE}} = \frac{1}{Q(i\omega)^n} \quad (1)$$

where i is an imaginary number, ω the angular frequency is 2π times the frequency of the AC signal ($\omega = 2\pi f$), Q is a measure of the magnitude of Z_{CPE} , and n is a constant within the range ($0 \leq n \leq 1$) [35]. When $n = 1$, Z_{CPE} is a purely capacitive impedance element, and Q is the capacitance; when $n = 0$, Z_{CPE} is a purely resistive element. For practical electrode–electrolyte interfaces, the CPE is used instead of a pure capacitance, accounting for the non-ideal capacitive behavior of the electrochemical double layer [18]. The Warburg impedance due to the diffusion of chemical reactants in the electrolyte is not included in this model, because when the EIS spectra for the interface were fitted with this circuit a low value was obtained for the Warburg impedance (~ 0.005) and it was considered negligible and removed from the circuit.

2.5.2. Cyclic voltammetry

Cyclic voltammetry (CV) was performed with a Gamry Reference 600 potentiostat using the same setup as described in the previous section. CV measurements were used to study the electrochemical processes that may occur on the TiN surface. The CV cycling was first performed between potential limits beyond the hydrolysis limits (-1 V and $+1.2$ V), represented in

a CV curve as large current peaks that correspond to dissolved gas and/or other reactions. The potential values before large current peaks are triggered define the *water window* limits. Since cycling outside of the safe limits is a destructive test for electrodes, this test was restricted to three electrodes of $80 \mu\text{m} \times 80 \mu\text{m}$ and three electrodes of $2 \text{mm} \times 80 \mu\text{m}$. The CV was then repeated within the no-hydrolysis limits to study the electrochemical behavior at a low sweep rate of 50mV s^{-1} . Provided the polarization of the stimulation (working) electrode during a pulse remains positive of the water reduction potential and negative of the water oxidation potential—within the water window—the stimuli charge density is often considered ‘safe’ [36].

2.5.3. Voltage transient measurements

Voltage transients were measured using cathodic-first, charge-balanced biphasic, symmetric square pulses delivered by a custom-built pulse stimulator. The acquisition of waveforms was performed with a digital oscilloscope (20MS s^{-1} sampling rate), using Origin® Lab for post-processing. The electrolyte type and the three-electrode configuration were the same as described for CV—the voltage is measured relative to Ag|AgCl. Voltage transient measurements were acquired for fifteen electrodes ($10 \times 6400 \mu\text{m}^2$, $5 \times 160000 \mu\text{m}^2$) from two wafers, using pulse widths of 50 and 200 μs. For the smaller electrodes, the charge per phase was varied between 3.2 and 11.5 nC, i.e. a minimum and maximum charge density of 50 and $180 \mu\text{C cm}^{-2}$, respectively. For the larger electrodes, the charge per phase was varied between 9.6 and 14 nC, meaning charge densities of 6 and $8.75 \mu\text{C cm}^{-2}$. For 50 μs pulses, the input current amplitude was varied between 64 and 300 μA, and for 200 μs pulses, it was varied between 16 and 80 μA. An interphase gap of 20 μs was used to stabilize the working electrode potential after cathodic phase offset. The electrodes were actively biased to 0 V between pulses. To determine the E_{mc} —the most negative potential after cathodic phase offset—it was decided to follow the approach of Leung *et al* [37], by using the potential near the end of the interphase gap, 15 μs after the end of cathodic phase, as the most approximate value between measured and real potential. Electrodes were stimulated for 3 min, and waveforms were acquired to ensure that the electrode voltage had reached a steady state.

3. Results

3.1. On-wafer TiN arrays

After wafer processing, the ready-to-release polyimide-based MEAs were obtained, as shown in figure 3(a). Here one can see the TiN MEA, the aluminum bond pads on the silicon die, the polyimide tabs ensuring the on-wafer device’s mechanical stability, and the mounting holes to be used for further device assembly. The polyimide tabs that hold the device after DRIE, and prevent it

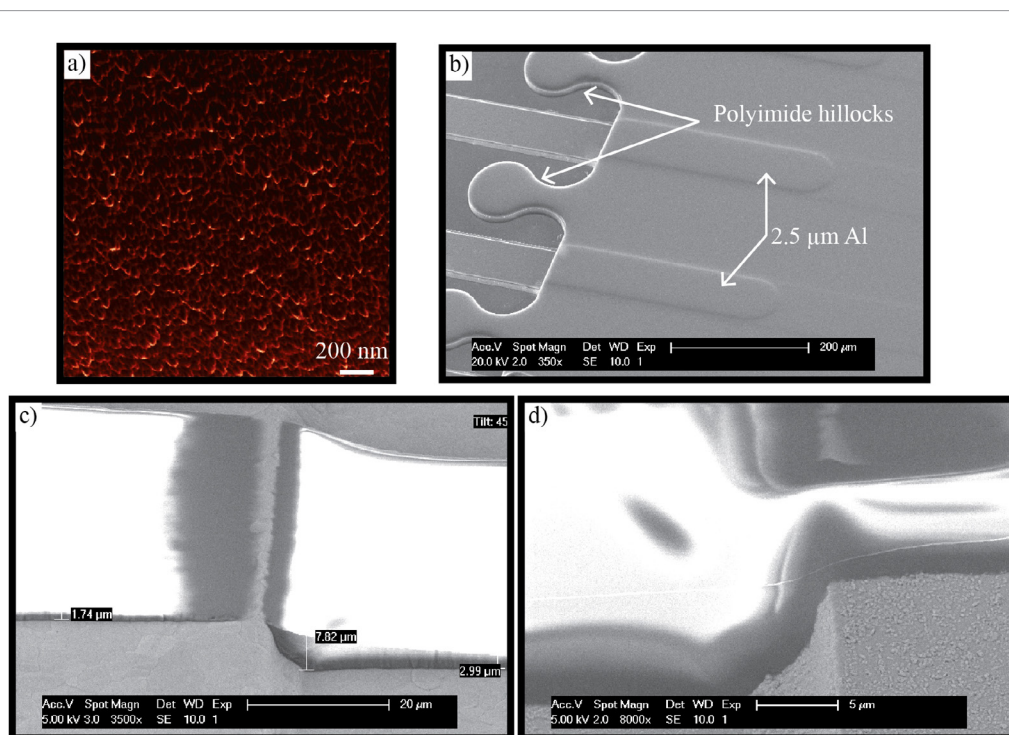


Figure 4. TiN surface characterization and silicon-to-polyimide transition. (a) Atomic force microscopy phase image of a 200 nm thick TiN coating, obtained by magnetron sputtering at 300 °C. Tapered crystallites of up to 100 nm in diameter, separated by voids. (b) Silicon-to-polyimide transition region, polyimide hillock structures to maximize overlapping area and increase mechanical resistance against delamination, and the 2.5 μm thick aluminum used for achieving good step coverage and, thus, good electrical connection. (c) 3 μm thick photoresist used for masking the aluminum layer proved insufficient in the transition region. (d) 4.5 μm thick photoresist layer used for masking aluminum.

from curling, can be cut parallel to the outer rim of the electrode substrate. The on-wafer prototypes can also be seen as supplementary data (stacks.iop.org/JNE/17/016010/mmedia). Before releasing it, the MEA was inspected with SEM. Figure 3(b) shows the 14-contact electrode array, and figure 3(c) shows one TiN microelectrode contact with vertical walls as well as the polyimide layer. The microelectrode is a linear array of 14 contacts, 2 mm in length. The edge length of each square electrode is 80 μm , and the inter-electrode pitch was set to 60 μm . By measuring devices processed in two different wafers, it was concluded that the fabricated MEA dimensions were within 3% of the design specifications. The cortical array is shown in figures 3(d) and (e), with 14 contacts of 2 mm \times 80 μm .

The sheet resistance of the Ti/TiN (40 nm/200 nm) film is 73.5 $\Omega \text{ sq}^{-1}$. The morphology of the sputtered TiN films was characterized by atomic force microscopy as shown in figure 4(a). The TiN is comprised of densely packed nodules and tapered crystallites that are approximately circular with a diameter of <100 nm. No hillocks or pyramidal-shaped structures were identified. Figure 4(b) shows the detail of the transition between regions without polyimide to regions with polyimide, on a silicon die. In order to achieve better mechanical resistance against delamination, polyimide hillocks were designed, thus maximizing the overlapped areas of polyimide on silicon. It also shows the 2.5 μm thick aluminum layer that was used to achieve optimal step coverage of interconnects

between deeper silicon dies and higher polyimide regions. Figures 4(c) and (d) depict the optimization of the photolithography process to pattern the 2.5 μm thick aluminum used for bond pads and for part of the interconnects. With a 3 μm thick photoresist (figure 4(c)), it was not possible to mask the aluminum layer. Satisfactory masking of the aluminum could only be achieved with a 4.5 μm thick photoresist as shown in figure 4(d).

3.2. Cuff assembly and usability test with dummies

The microdevice was released from the wafer by cutting its polyimide tables. Wire bonding was done from the aluminum pads on the silicon chip to the gold pads on the PCB. The connector was welded to the PCB beforehand. By using the mounting holes as fixation and alignment structures, the polyimide foils were glued to pre-molded PDMS cuffs using the silicone adhesive MED 2000 from NuSil. Two examples of split-cylinder cuffs with polyimide-based MEAs are shown in figure 5. The molding tool is used to cast the PDMS around the silicon die, bonding wires and the PCB. This protective block of PDMS minimizes the risk of damaging the fragile bonding wires, and short circuits when immersing the device in saline solution for electrochemical characterization or in *in vivo* use.

3.3. Electrode impedance performance

Figures 6(a) and (b) show the EIS spectra of the twenty TiN microelectrodes (80 μm \times 80 μm). The samples exhibit a time constant behavior, i.e. a capacitive

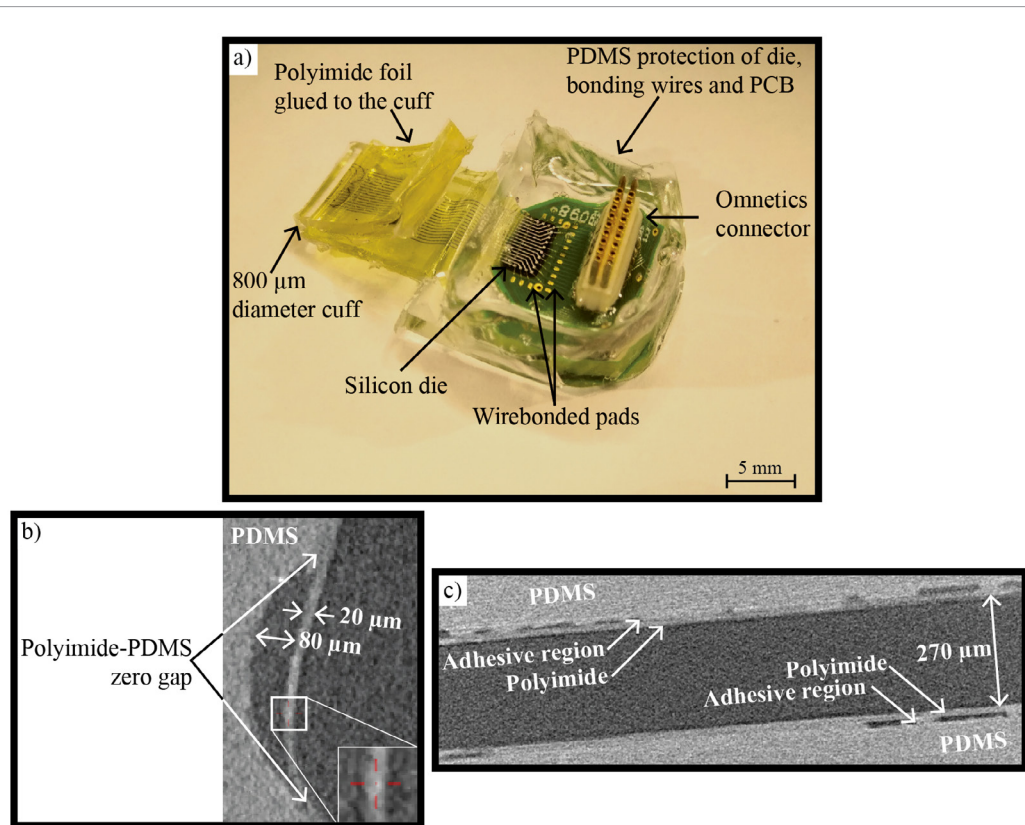


Figure 5. Split-cylinder cuff with integrated polyimide-based MEA. (a) Fully assembled electrode with visible yellow polyimide foils through transparent PDMS cuffs. Bonding wires connecting pads on silicon die to pads on PCB are also visible. An 18 pin Omnetics neuro-connector as interface with the external electronics. (b) Micro-CT, transversal plane of the cuff electrode, detailing its cylindrical portion. Polymers (PDMS and polyimide) are light gray and air is dark gray. The polyimide foil is $20\ \mu\text{m}$ thick and the maximum gap between PDMS and polyimide foil is $80\ \mu\text{m}$. Close to that maximum value, the gap between polyimide and PDMS decreases. (c) Micro-CT of the horizontal portion of the cuff electrode (between electrode contacts and silicone die). Silicone adhesive exists in a large extension of the PDMS–polyimide interface, alongside some small void regions. Gap between polyimide and PDMS is lower than $20\ \mu\text{m}$, and the separation between the two stripes is $270\ \mu\text{m}$.

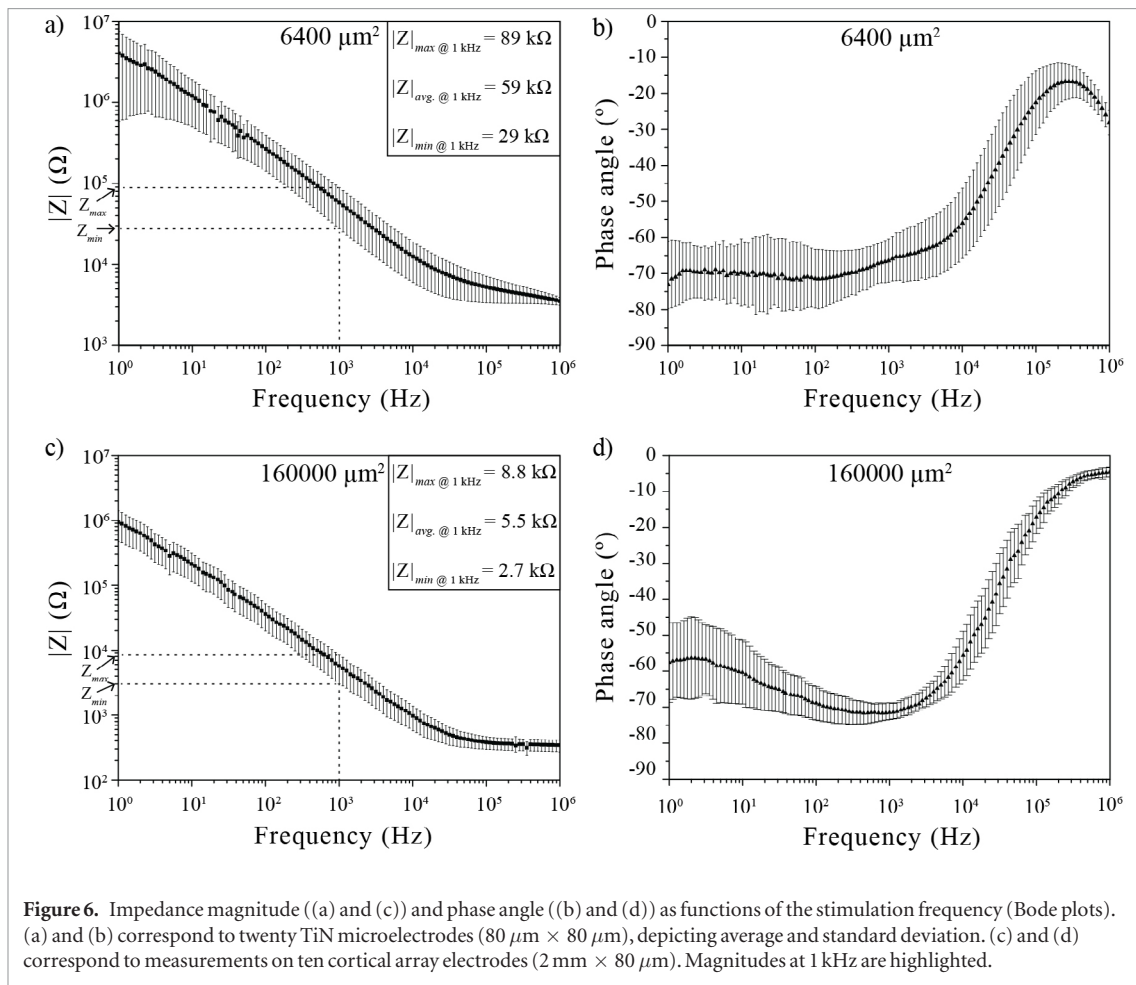
response in parallel with a resistive response, which is typical for a metal–electrolyte interface. Impedance behavior can be analyzed over three distinct ranges of frequency: (1) low-frequency region (below 100 Hz), where $|Z| = R_p + R_e$, with dominant polarization resistance; (2) mid-frequency region between 100 Hz and 10 kHz with nearly linear dependence between the magnitude and stimulation frequency; and (3) above 10 kHz, where the magnitude is less frequency-dependent, the total impedance is close to the electrolyte’s resistance (R_e), and phase angle increases to close to -10° (indicative of resistive charge transfer) [19]. Impedance magnitude at 1 kHz is $59 \pm 30\ \text{k}\Omega$, and the phase angle ranges between -60 and -80° indicating predominant capacitive coupling. The EIS spectra of cortical array electrodes (figures 6(c) and (d)) show a similar behavior to that of the microelectrodes, with a slightly prolonged resistive region in the upper frequencies, and with lower impedance magnitudes overall. Impedance magnitude at 1 kHz is $5.5 \pm 3\ \text{k}\Omega$, and the phase angle up to 1 kHz also reveals a capacitive coupling.

Of the two MEA devices from two different wafers tested under EIS (i.e. a total of 28 electrode contacts), eight electrode contacts exhibited higher impedance magnitudes ($|Z|_{1\ \text{kHz}} > 500\ \text{k}\Omega$) with associated phase

rotations (phase angle near zero degrees below 1 kHz). This is indicative of a deficient electrode–electrolyte interface, when compared to fully functional interfaces. These electrodes were then disabled and not used for further testing. The ten cortical array electrodes tested in a flat configuration (no cuff assembly) were all from the same device. No indications of deficient interfaces were found, as all impedance magnitudes at 1 kHz were lower than $8.8\ \text{k}\Omega$.

3.3.1. Fitting EIS spectra

The EIS spectra of TiN microelectrodes, shown in figure 5, were fitted to the equivalent circuit described in section 2.5.1, and the following fitting parameters were obtained: interfacial capacitance ($Q = 2.03 (10^{-8})\ \text{s}\Omega^{1/n}$), polarization resistance ($R_p = 2.3 \times 10^{11}\ \Omega\ \text{cm}^{-2}$), electrolyte resistance ($R_e = 3500\ \Omega$), and $n = 0.78$. Using the empirical relation from (1) and the fitting parameters $Q = 2.03 (10^{-8})\ \text{s}\Omega^{1/n}$, $n = 0.78$, the theoretical, non-Faradaic impedance at 1 kHz is $56\ \text{k}\Omega$. This value corresponds to the interface capacitance and deviates by about 5% from the (mean value of) measured impedance magnitudes: $59\ \text{k}\Omega$. The fitted value of $n = 0.78$ indicates some deviation from the ideal capacitive response ($n = 1$).



3.4. Cyclic voltammetry

The TiN voltammograms, obtained at a slow sweep rate of $50\ \text{mV s}^{-1}$, are illustrated in figure 7. CV between $-1\ \text{V}$ and $1.2\ \text{V}$ indicates a typical TiN voltammogram profile with no distinct current peaks around zero potential and sharp increases in both cathodic and anodic currents beyond certain limits, as shown in figure 6(a). The peaks in the cathodic direction, below $-0.6\ \text{V}$, may be attributed to the reduction of titanium dioxide with nitrogen formation [38], leading to the absorption of hydrogen into the oxide and increased conductivity [18]. The peaks in the anodic direction (more positive than $0.8\ \text{V}$) may be the oxidation of the reduced oxide. The decrease and stabilization of current densities in the oxidation peaks of cycles 1, 5 and 10 mean that the oxide growth achieves a stable thickness. These limits of $-0.6\ \text{V}$ and $0.8\ \text{V}$ are safe potential limits, defining the so-called *water window* region, and are consistent with those reported previously [19]. Cycling the TiN electrodes between them guarantees that the charge injection occurs through non-Faradaic or capacitive reactions, i.e. with reversible redistribution of charge.

Investigation of electrochemical reactions for potentials between $-0.6\ \text{V}$ and $0.8\ \text{V}$ confirms a rectangular-like shape indicative of the capacitive behavior (figures 7(b) and (c)). Small current peaks are visible in the anodic sweep of (b), which point to some oxidation processes, with the growth of titanium

dioxide taking place at the cost of the nitride as oxygen atoms penetrate the coating and replace the nitrogen atoms [18]. The absence of current peaks in the larger cortical electrodes (figure 7(c)) suggests less penetration in its TiN pores, thus limiting redox reactions.

3.5. Voltage transient measurements

The voltage transients were recorded and used to determine pulse parameters (amplitude, width) driving E_{mc} values to almost $-0.6\ \text{V}$. This allowed us to determine the safe charge injection limits of the ten microelectrodes ($80\ \mu\text{m} \times 80\ \mu\text{m}$) and five cortical electrodes ($2\ \text{mm} \times 80\ \mu\text{m}$). Figure 8 shows the voltage transients of one TiN microelectrode for pulse widths of 50 and $200\ \mu\text{s}$; figures 8(a) and (b), respectively. To ease interpretation, the plots of two voltage excursions are shown, corresponding to two values of charge, instead of all charge steps tested. For the electrode shown, the maximum negative potential, E_{mc} , is $-0.25\ \text{V}$ and $-0.55\ \text{V}$, respectively, for $3.2\ \text{nC}$ and $9.6\ \text{nC}$ per phase. The access voltage, V_{a} , is higher when using higher current amplitudes, leading to lower driving voltages. However, that does not change the maximum negative potential on the microelectrode at the end of the interphase gap. All ten microelectrodes, from two different wafers, used in these experiments show similar voltage transient profiles. Maximum charge densities between 130 and $180\ \mu\text{C cm}^{-2}$ drive the E_{mc} levels close to $-0.6\ \text{V}$ in the ten electrodes. The charge

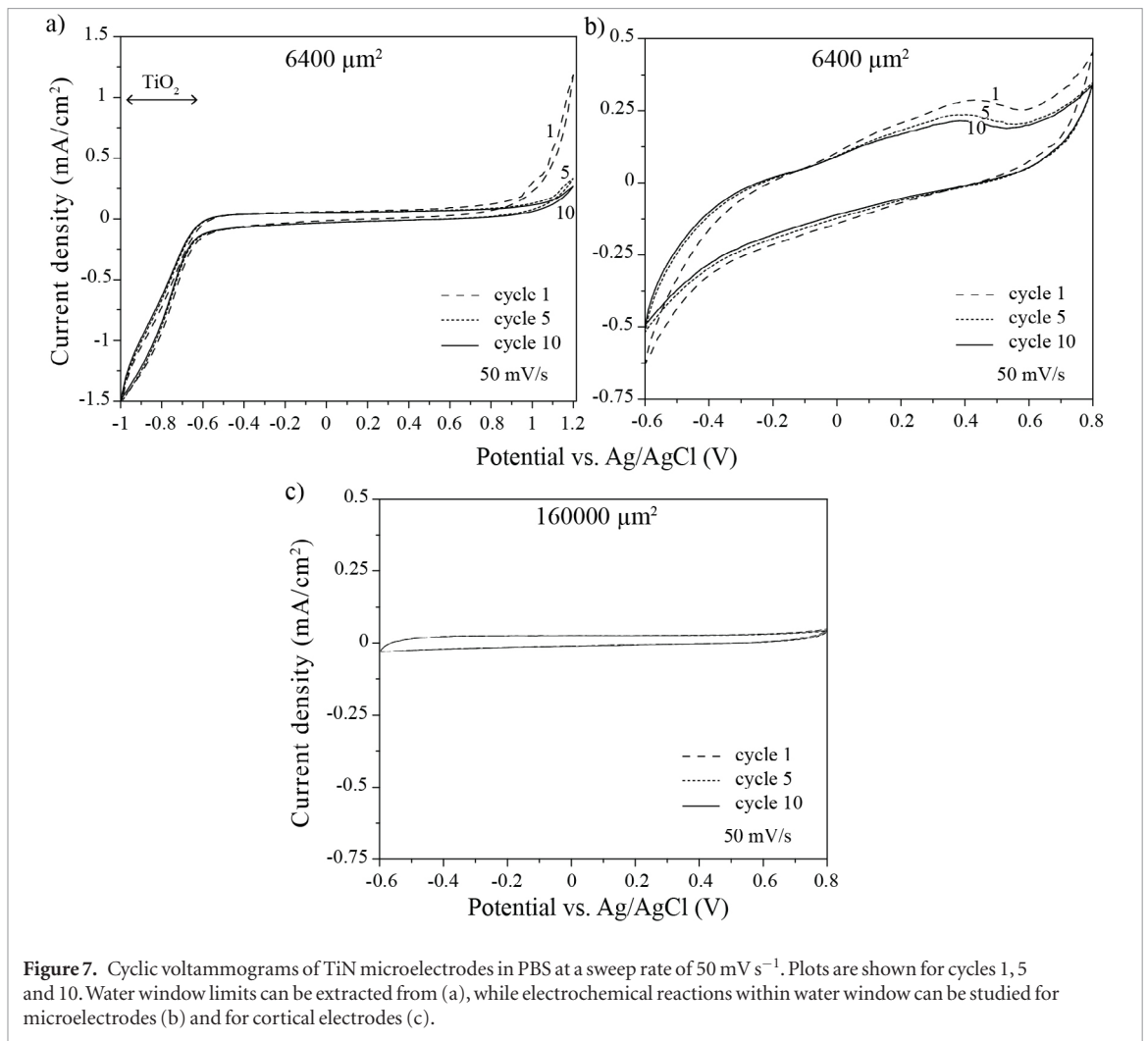


Figure 7. Cyclic voltammograms of TiN microelectrodes in PBS at a sweep rate of 50 mV s^{-1} . Plots are shown for cycles 1, 5 and 10. Water window limits can be extracted from (a), while electrochemical reactions within water window can be studied for microelectrodes (b) and for cortical electrodes (c).

injection capacity, Q_{inj} , of the TiN microelectrodes is then determined to be $154 \pm 16 \mu\text{C cm}^{-2}$.

The voltage transients for five cortical array electrodes are shown in figures 8(c) and (d), respectively, for pulse widths of 50 and 200 μs . Maximum charge densities between 8.25 and 8.75 $\mu\text{C cm}^{-2}$ drive the E_{mc} levels to close to -0.6 V in the five electrodes. The charge injection capacity, Q_{inj} , of the TiN cortical array electrodes is then $8.5 \pm 0.19 \mu\text{C cm}^{-2}$.

4. Discussion

Here, we present a newly developed microfabrication method for manufacturing high-density TiN MEAs on flexible substrates. Customization is possible since TiN MEAs, polyimide foils and silicon chips of arbitrary shape can be realized. Furthermore, integration of a higher density of contacts is possible and is discussed below. In the present work, each TiN microelectrode has an area of $6400 \mu\text{m}^2$, and is grouped in a 14-contact array with 2 mm length. The polyimide-based TiN MEAs were mounted onto split-cylinder cuffs, and micro-CT scans of an assembled device showed good adhesion between the PDMS and the polyimide, with no gaps in a large percentage of glued areas and with short void regions. Most of these gaps between the

PDMS and polyimide are under $20 \mu\text{m}$, and in one localized spot at the cylindrical shaped cuff the gap is as much as $80 \mu\text{m}$. This same device was used for electrochemical characterization and its performance has not been jeopardized by the presence of those voids or gaps, even after extensive manipulation of the electrode (opening and closing) for the removal of air bubbles. Detachment of polyimide from PDMS has not been observed.

The inner diameter of the cuff ranges between 600 and 700 μm , making it suitable for sub-millimeter neural applications, e.g. in the rat vagus nerve with diameters between 200–400 μm [39]. In that case, the distance between the electrode and nerve is expected to be between 50 and 250 μm , which are typical distances between extraneural electrodes and nerves. Lertmanorath *et al* [40] showed selective stimulation of the cat gastrocnemius nerve ($0.3 \text{ mm} \times 1.2 \text{ mm}$) with a flat interface nerve electrode (FINE) of 0.5 mm opening, i.e. gap nerve/electrode of 100 μm , and Yu *et al* [24] showed selective recruitment of fascicles in the rat sciatic nerve ($1.6 \text{ mm} \times 1.2 \text{ mm}$) using a 1.7 mm diameter cuff, i.e. gap nerve/electrode of 250 μm .

We have determined the *in vitro* electrochemical properties of sputtered TiN layers, namely its impedance spectra, cyclic voltammograms and voltage tran-

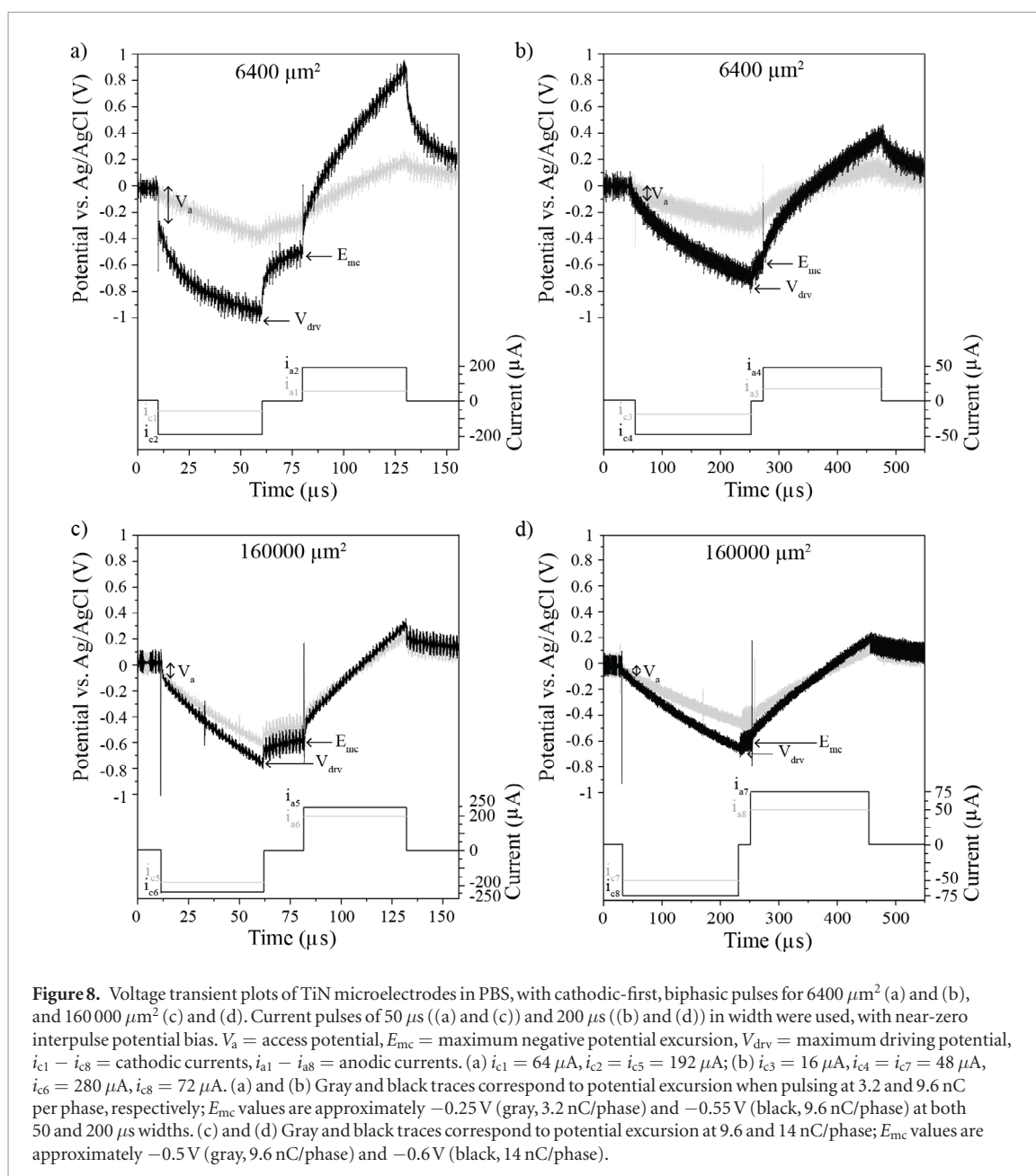


Table 1. Geometrical and electrochemical properties of reference works and of present work.

GSA	Impedance @ 1 kHz	Water window	Charge injection capacity	Reference
$4000 \mu\text{m}^2$	20–30 k Ω	-0.6 V to $+0.8 \text{ V}$	$550 \mu\text{C cm}^{-2}$ @ 200 μs cathodic	Weiland et al [19]
6 mm^2	242 k Ω (smooth) 203 k Ω (porous)	-0.6 V to $+1 \text{ V}$	$24 \mu\text{C cm}^{-2}$ @ 200 μs cathodic (smooth)	Meijs et al [20]
$13500\text{--}139500 \mu\text{m}^2$	1–3 k Ω	-0.6 V to $+0.8 \text{ V}$	$500 \mu\text{C cm}^{-2}$ @ 200 μs cathodic	González-González et al [41]
$6400 \mu\text{m}^2$	29–89 k Ω	-0.6 V to $+0.8 \text{ V}$	$154 \mu\text{C cm}^{-2}$	Present work
$160000 \mu\text{m}^2$	2.7–8.8 k Ω		$8.5 \mu\text{C cm}^{-2}$ @ 200 μs cathodic	

sient measurements. Values of interest such as the impedance magnitude (including values at 1 kHz) and phase, water window or safe potential limits, and charge injection capacity were extracted. A comparative analysis between the present work and literature is done below on the electrochemical behavior of TiN micro- and macroelectrodes and relevant values are discussed. An overview is shown in Table 1.

4.1. Miniaturization, customization and contact density potential

Next, the potential of the proposed microfabrication methodology is analyzed as an enabler of miniaturization and integration, as well as a driver for higher density of contacts. The interconnection solution presented in figure 4 was adopted since it was required to have direct access to the electrodes for characterization, leading to a device with a size comparable to other electrode systems used in acute animal experiments [25, 42]. However, the device can be significantly reduced in size if, instead of using the bulky connector attached to the PCB, the silicon die is used as a platform to enable the use of MEMS integration and packaging technologies. Since electrodes are routed and accessible on top of a silicon die, several technologies are available to integrate the developed electrode with electronics [43]. On a silicon wafer, self-assembling can be used to integrate multiple chips on a full wafer [44].

In the current device, the pitch between electrodes was set to 60 μm . By setting the pitch to 5 μm , a total of 24 electrodes could be patterned in a 2 mm long space, meaning an increment from the current 14×1 array to a 24×1 array, keeping the same electrode area. However, such increase in the overall number of electrodes brings up new design challenges related to the dimensions of the PCB used as an interface with the outside. In the present design, a 10 mm wide PCB is enough to interface with 14 contacts. If more electrodes are to be used, judicious evaluation of the number of electrodes is required together with size constraints of the overall probe.

4.2. Microfabrication process reproducibility

Reproducibility of the fabrication process is defined as the closeness of electrochemical measures across different processed wafers. Twenty-eight microelectrodes ($80 \mu\text{m} \times 80 \mu\text{m}$) from two wafers have been characterized in terms of electrochemical impedance spectroscopy. At 1 kHz, the impedance magnitudes ranged between 29 and 89 k Ω and the phase angle between -60 and -80° . Ten microelectrodes from two wafers have been characterized in terms of the voltage transients. The charge injection capacity of microelectrodes is $154 \mu\text{C cm}^{-2}$ (9.9/phase). Ten cortical array electrodes ($2 \text{ mm} \times 80 \mu\text{m}$) from one wafer were characterized in terms of the EIS. At 1 kHz, the impedance magnitudes ranged between 2.7 and 8.8 k Ω . Such inverse correlation between the area and

impedance magnitude has been systematically found for TiN electrodes. Also, for the larger cortical array electrodes, the charge injection capacity has been found to be $8.5 \mu\text{C cm}^{-2}$, i.e. 13.6 nC/phase. The charge injection capacity thus decreases as the area increases. A similar finding has been reported by Cogan *et al* for SIROF electrodes [9]. As these correlations between area and electrochemical measures were systematic across all measurements made, the microfabrication process is considered reproducible.

Applications that require charge per phase of up to 10 nC per phase—such as those allowed by current TiN microelectrodes—include microstimulation of pudendal afferent fibers to elicit the reflex bladder sensation (up to 5 nC per phase with Utah microelectrodes) [45], intracortical microstimulation of the somatosensory cortex to restore hand tactile sensation (with 10 nC per phase with Utah microelectrodes) [46], and the use of cuff electrodes for reconstructing electrical impedance tomography images of fascicular activation within the sciatic nerve and using charges of up to 5 nC per phase [47].

The underlying reasons for the significant increases in impedance magnitude and changes of the phase angle in 8 out of the 28 electrodes tested in EIS are associated with the cuff assembly process. Stress induced on the polyimide-based microelectrodes when maneuvering and gluing them onto the pre-molded PDMS led to changes in the mechanical properties of the metal routings (electrodes and/or interconnects), ultimately leading to changes in the electrochemistry of those eight electrode contacts. One possible solution to avoid damaging of contacts could be to use alternative methods for cuff forming, e.g. temperature tempering with metal rods [55] or *in situ* suturing [54]. However, those methods present disadvantages in terms of handling, lacking the dedicated handling structures that the current work proposes. The polyimide-based TiN microelectrodes presented in this work may also be used as cortical arrays, i.e. without cuff assembly, thus preventing stress-induced undesired effects.

4.3. Electrical property suitability of sputtered TiN microelectrodes for recording and stimulation

The impedance magnitude and phase of TiN MEAs follow typical profiles previously described in the literature for ‘smooth’ TiN electrodes [11, 15, 18, 20]. From the fitting of impedance spectra, the electrolyte’s resistance is 3500 Ω . If the equation proposed by Franks *et al* [34], $R_s = \rho_{\text{PBS}}/4r$, and microelectrodes are approximated to circles of $r = 40 \mu\text{m} = 0.004 \text{ cm}$, then the electrolyte resistance equals 3875 Ω . The impedance magnitude is close to the electrolyte resistance (R_e) in the high frequencies, while increasing nearly linearly in the mid- to low frequencies. On the contrary, ‘rough’ or ‘porous’ TiN films have low, near- R_e frequencies almost across the entire frequency spectrum. The morphology of both smooth and

porous TiN films is the underlying reason for those differences. The electrochemical surface areas of smooth TiN films are lower when compared to those of the porous layers. Considering a transmission line model of pores, such as the one described by Norlin *et al* [18], it is clear that, at low and mid-frequencies, deeper pore surface areas come increasingly into play for charge transfer, thus contributing to lower impedance magnitudes. At higher frequencies, the impedance magnitude approximates to the electrolyte's resistance regardless of film porosity.

Electrode impedance magnitude measured at 1 kHz in a saline solution is regularly used as a proxy for its ability to record neuronal activity. In the present work, 20 TiN microelectrodes of $6400 \mu\text{m}^2$ yield magnitude impedances between 29 and 89 k Ω at 1 kHz. $177 \mu\text{m}^2$ iridium electrodes with an impedance magnitude of 100 k Ω at 1 kHz have successfully been used for single unit recording in rat brains [48]. In another study [49], rough-surfaced AuPt nanoparticles with an area of $2870 \mu\text{m}^2$ and an average impedance of 230 k Ω at 1 kHz were used for the recording of spontaneous spike signals in rats.

The water window or safe potential limits of the sputtered TiN microelectrodes in the present work were found to be -0.6 V and $+0.8 \text{ V}$, the same as reported by Weiland *et al* [19]. In their work, TiN electrode contacts with a geometric surface area (GSA) of $4000 \mu\text{m}^2$, pulsed in PBS with 200 μs long pulses, resulted in a Q_{inj} of $550 \mu\text{C cm}^{-2}$, comparatively higher than in the present study. Rigid, silicon-based probes, including low-pressure chemical vapor deposition (LPCVD) phosphorus-doped polysilicon as a conductor layer, were used as a support to the sputtered TiN electrodes. When deposited directly on a highly conformal pinhole-free layer such as the LPCVD polysilicon, the porosity of PVD TiN is increased, compared to when TiN is deposited on an underlying PVD layer [17], which is the case in the current work. TiN layers with high porosity yield a higher charge injection capacity [20]. Additionally, LPCVD phosphorus-doped polysilicon has a sheet resistance as low as $2 \Omega \text{ sq}^{-1}$ [50], providing lower resistivity interconnects when compared to the sputtered TiN in the present work (sheet resistance of $73.5 \Omega \text{ sq}^{-1}$). LPCVD uses, however, temperatures above $600 \text{ }^\circ\text{C}$, which is the decomposition temperature of polyimide [51]. Thus, a high-temperature process like LPCVD was not an option for the present microfabrication method.

In a recent study, Meijs *et al* used a titanium alloy ($\text{Ti}_6\text{Al}_4\text{V}$) rigid pin as an underlying layer for the sputtering of TiN macroelectrodes with an area of 6 mm^2 [20]. A $10 \mu\text{m}$ thick TiN layer was deposited in two different stoichiometric conditions, yielding 'smooth' and 'porous' films, analyzed both *in vitro* and *in vivo*. Voltammograms of both the smooth and porous TiN electrodes showed a water window between -0.6 V and $+1 \text{ V}$ and a rectangular shaped (capacitive) profile, with no distinctive peaks in either of them.

The Q_{inj} of smooth TiN macroelectrodes in PBS was $24 \pm 4 \mu\text{C cm}^{-2}$, but no result was given for the *in vivo* condition. In general, porous electrode layers yield electrically active areas larger than the corresponding GSA, which in turn results into a larger charge injection capacity.

In 2018, González-González *et al* [41] introduced the use of a shape memory polymer (SMP) in the fabrication of multi-electrode softening cuffs. A 220 nm thick TiN (TiN) layer is deposited over a 300 nm thick Au layer by RF sputtering. The TiN and Au interconnects are patterned by standard photolithography and wet-etching methods and are sandwiched between two layers of SMP, that is deposited by spin-coating and cured by photo-polymerization. TiN electrode designs have been manufactured to target final diameters between 100 μm and 1 mm. For TiN contacts of GSA between 13 500 and 139 500 μm^2 , impedances are between 1 and 3 k Ω , and the Q_{inj} is $500 \mu\text{C cm}^{-2}$ for 200 μs cathodic pulses. Water window limits are reported between -0.6 V and $+0.8 \text{ V}$.

In the present study, the Q_{inj} of ten TiN microelectrodes ranges between 130 and 180 $\mu\text{C cm}^{-2}$, which over a GSA of $6.4 \times 10^{-5} \text{ cm}^2$ means a total charge per phase of 8 nC to 11.5 nC, within the safe potential limits. TiN MEAs may then be used in assembled cuffs for electrical impedance tomography applications in the rat vagus nerve, or they may be used in an unrolled state for cortical microstimulation.

5. Conclusion

In this work, we present a novel microfabrication technology based on MEMS and CMOS processing techniques and materials able to deliver TiN MEAs on flexible substrates. TiN MEAs are ready for recording and stimulation, in their out-of-the-wafer 'planar' structure or in combination with split-cylinder cuffs designed for the rat vagus nerve. The TiN microelectrodes have a comparable electrochemical performance to other state-of-the-art devices. This technology aims to integrate electronic modules for on-chip stimulation and recording.

Acknowledgments

This work was supported by the FCT (Portuguese Foundation for Science and Technology) under projects PTDC/EEL-TEL/5250/2014—POCI01-145-FEDER-16695, by FEDER funds through Projeto 3599—Promover a Produção Científica e Desenvolvimento Tecnológico e a Constituição de Redes Temáticas (3599- PPCDT), Grant SFRH/BD/62608/2009, and the project CMEMS reference UID/EEA/04436/2019. The authors gratefully thank Bruno Morana and Gregory Pandraud from ECTM/TU Delft for generous support in the CVD and photolithography processes, and Pascale Pham from CEA-LETI for discussions about electrochemical impedance spectroscopy.

ORCID iDs

F Rodrigues  <https://orcid.org/0000-0002-7040-9843>

P M Mendes  <https://orcid.org/0000-0003-2177-7321>

References

- [1] Wang R, Yu H and Li Z 2018 Microelectrode array *Micro Electro Mechanical Systems* (Singapore: Springer) pp 1379–411
- [2] Nordhausen C T, Maynard E M and Normann RA 1996 Single unit recording capabilities of a 100 microelectrode array *Brain Res.* **726** 129–40
- [3] Branner A and Normann RA 2000 A multielectrode array for intrafascicular recording and stimulation in sciatic nerve of cats *Brain Res. Bull.* **51** 293–306
- [4] Wark H A C et al 2013 A new high-density (25 electrodes mm^{-2}) penetrating microelectrode array for recording and stimulating sub-millimeter neuroanatomical structures *J. Neural Eng.* **10** 045003
- [5] Rodríguez F J, Ceballos D, Schuttler M, Valero A, Valderrama E, Stieglitz T and Navarro X 2000 Polyimide cuff electrodes for peripheral nerve stimulation *J. Neurosci. Methods* **98** 105–18
- [6] Lu Y, Lyu H, Richardson A G, Lucas T H and Kuzum D 2016 Flexible neural electrode array based-on porous graphene for cortical microstimulation and sensing *Sci. Rep.* **6** 1–9
- [7] Ji B, Guo Z, Wang M, Yang B, Wang X, Li W and Liu J 2018 Flexible polyimide-based hybrid opto-electric neural interface with 16 channels of micro-LEDs and electrodes *Microsyst. Nanoeng.* **4** 1–11
- [8] Stieglitz T and Gross M 2002 Flexible BIOMEMS with electrode arrangements on front and back side as key component in neural prostheses and biohybrid systems *Sensors Actuators B* **83** 8–14
- [9] Cogan S F, Ehrlich J, Plante T D, Smirnov A, Shire D, Gingerich M and Rizzo J 2009 Sputtered iridium oxide films for neural stimulation electrodes *J. Biomed. Mater. Res. B* **89** 353–61
- [10] Gillis W F et al 2018 Carbon fiber on polyimide ultra-microelectrodes *J. Neural Eng.* **15** 219–27
- [11] Cogan S F 2008 Neural stimulation and recording electrodes *Annu. Rev. Biomed. Eng.* **10** 275–309
- [12] Lukosius M, Wenger C, Pasko S, Mussig H J, Seitzinger B and Lohe C 2008 Atomic vapor deposition of titanium nitride as metal electrodes for gate-last CMOS and MIM devices *Chem. Vap. Depos.* **14** 123–8
- [13] Lawand N S, Zeijl H V, French P J, Briaire J J and Frijns J H M 2013 Titanium nitride (TiN) as a gate material in BiCMOS devices for biomedical implants *Proc. IEEE Sensors* pp 1482–6
- [14] Janders M, Egert U, Stelzle M and Nisch W 1996 Novel thin film titanium nitride micro-electrodes with excellent charge transfer capability for cell stimulation and sensing applications *18th Annual Int. Conf. of the IEEE Eng. Med. Biol. Soc.* pp 245–7
- [15] Pedrosa P, Alves E, Barradas N P, Fiedler P, Hauelsen J, Vaz F and Fonseca C 2012 TiN_x coated polycarbonate for bio-electrode applications *Corros. Sci.* **56** 49–57
- [16] Cunha L T, Pedrosa P, Tavares C J, Vaz F, Fonseca C and Alves E 2009 The role of composition, morphology and crystalline structure in the electrochemical behaviour of TiN_x thin films for dry electrode sensor materials *Electrochim. Acta* **55** 59–67
- [17] Tato W and Landolt D 1998 Electrochemical determination of the porosity of single and duplex PVD coatings of titanium and titanium nitride on brass *J. Electrochem. Soc.* **145** 4173–81
- [18] Norlin A, Pan J and Leygraf C 2005 Investigation of electrochemical behavior of stimulation/sensing materials for pacemaker electrode applications *J. Electrochem. Soc.* **152** J7–15
- [19] Weiland J D, Anderson D J and Humayun M S 2002 *In vitro* electrical properties for iridium oxide versus titanium nitride stimulating electrodes *IEEE Trans. Biomed. Eng.* **49** 1574–9
- [20] Meijs S, Sørensen C, Sørensen S, Rechendorff K, Fjorback M and Rijkhoff N J M 2016 Influence of implantation on the electrochemical properties of smooth and porous TiN coatings for stimulation electrodes *J. Neural Eng.* **13** 026011
- [21] Veraart C, Grill W M and Mortimer J T 1993 Selective control of muscle activation with a multipolar nerve cuff electrode *IEEE Trans. Biomed. Eng.* **40** 640–53
- [22] Nielsen T N, Kurstjens G A M and Struijk J J 2011 Transverse versus longitudinal tripolar configuration for selective stimulation with multipolar cuff electrodes *IEEE Trans. Biomed. Eng.* **58** 913–9
- [23] Lee S H, Jung J H, Chae Y M, Suh J K F and Kang J Y 2010 Fabrication and characterization of implantable and flexible nerve cuff electrodes with Pt, Ir and IrOx films deposited by RF sputtering *J. Micromech. Microeng.* **20** 035015
- [24] Yu H, Xiong W, Zhang H, Wang W and Li Z 2014 A parylene self-locking cuff electrode for peripheral nerve stimulation and recording *J. Microelectromech. Syst.* **23** 1025–35
- [25] Kang X, Liu J Q, Tian H, Yang B, Nuli Y and Yang C 2015 Self-closed parylene cuff electrode for peripheral nerve recording *J. Microelectromech. Syst.* **24** 319–32
- [26] Fitzgerald J J, Lago N, Benmerah S, Serra J, Watling C P, Cameron R E, Tarte E, Lacour S, McMahon S B and Fawcett J W 2012 A regenerative microchannel neural interface for recording from and stimulating peripheral axons *in vivo* *J. Neural Eng.* **9** 016010
- [27] Plachta D T T, Gierthmuehlen M, Cota O, Espinosa N, Boeser F, Herrera T, Stieglitz T and Zentner J 2014 Blood pressure control with selective vagal nerve stimulation and minimal side effects *J. Neural Eng.* **11** 036011
- [28] Polasek K H, Hoyer H, Keith M W, Kirsch R F and Tyler D T 2009 Stimulation stability and selectivity of chronically implanted multicontact nerve cuff electrodes in the human upper extremity *IEEE Trans. Neural Syst. Rehabil. Eng.* **17** 428–37
- [29] Behkami S, Frounchi J, Pakdel F G and Stieglitz T 2018 Simulation of effects of the electrode structure and material in the density measuring system of the peripheral nerve based on micro-electrical impedance tomography *Biomed. Eng.* **63** 151–61
- [30] Myllymaa S, Myllymaa K, Korhonen H, Töyräs J, Jääskeläinen J E, Djupsund K, Tanila H and Lappalainen R 2009 Fabrication and testing of polyimide-based microelectrode arrays for cortical mapping of evoked potentials *Biosens. Bioelectron.* **24** 3067–72
- [31] Tolstosheeva E, Gordillo-González V, Biefeld V, Kempen L, Mandon S, Kreiter A K and Lang W 2015 A multi-channel, flex-rigid ECoG microelectrode array for visual cortical interfacing *Sensors* **15** 832–54
- [32] Mimoun B, Pham H T M, Henneken V and Dekker R 2013 Residue-free plasma etching of polyimide coatings for small pitch vias with improved step coverage *J. Vac. Sci. Technol. B* **31** 021201
- [33] Rodrigues F and Mendes P 2014 A new integration method for mounting and *in vivo* handling of sub-mm flexible cuff electrode *Proc. of the Int. Conf. on Biomedical Electronics and Devices* pp 265–70
- [34] Franks W, Schenker I, Schmutz P and Hierlemann A 2005 Impedance characterization and modeling of electrodes for biomedical applications *IEEE Trans. Biomed. Eng.* **52** 1295–302
- [35] Norlin A, Pan J and Leygraf C 2002 Investigation of interfacial capacitance of Pt, Ti and TiN coated electrodes by electrochemical impedance spectroscopy *Biomol. Eng.* **19** 67–71
- [36] Cogan S F, Garrett D J and Green R A 2016 Electrochemical principles of safe charge injection *Neurobiotics: the Biomedical Engineering of Neural Prostheses* (New York: Wiley) pp 55–88
- [37] Leung R T, Shivdasani M N, Nayagam D A X and Shepherd R K 2015 *In vivo* and *in vitro* comparison of the charge injection

- capacity of platinum macroelectrodes *IEEE Trans. Biomed. Eng.* **62** 849–57
- [38] Bellanger G and Rameau JJ 1995 Corrosion of titanium nitride deposits on AISI 630 stainless steel used in radioactive water with and without chloride at pH 11 *Acta Electrochim.* **40** 2519–32
- [39] Alcántara A C L, Salgado H C and Fazan V P S 2008 Morphology and morphometry of the vagus nerve in male and female spontaneously hypertensive rats *Brain Res.* **1197** 170–80
- [40] Lertmanorat Z, Gustafson K J and Durand D M 2006 Electrode array for reversing the recruitment order of peripheral nerve stimulation: experimental studies *Ann. Biomed. Eng.* **34** 152–60
- [41] González-González M A et al 2018 Thin film multi-electrode softening cuffs for selective neuromodulation *Sci. Rep.* **8** 16390
- [42] Lee Y J, Kim H J, Do S H, Kang J Y and Lee S H 2016 Characterization of nerve-cuff electrode interface for biocompatible and chronic stimulating application *Sensors Actuators B* **237** 924–34
- [43] Fischer A C, Forsberg F, Lapisa M, Bleiker S J, Stemme G, Roxhed N and Niklaus F 2015 Integrating MEMS and ICs *Microsyst. Nanoeng.* **1** 15005
- [44] Fukushima T, Iwata E, Ohara Y, Murugesan M, Bea J, Lee K, Tanaka T and Koyanagi M 2012 Multichip-to-wafer three-dimensional integration technology using chip self-assembly with excimer Lamp irradiation *IEEE Trans. Electron Devices* **59** 2956–63
- [45] Bruns T M, Weber D J and Gaunt R A 2014 Microstimulation of afferents in the sacral dorsal root ganglia can evoke reflex bladder activity *Neurorol. Urodyn.* **34** 65–71
- [46] Flesher S N, Collinger J L, Foldes S T, Weiss J M, Downey J E, Tyler-Kabara E C, Bensmaia S J, Schwartz A B, Boninger M L and Gaunt R A 2016 Intracortical microstimulation of human somatosensory cortex *Sci. Transl. Med.* **8** 361ra141
- [47] Aristovich K, Donegá M, Blochet C, Avery J, Hannan S, Chew D J and Holder D 2018 Imaging fast neural traffic at fascicular level with electrical impedance tomography: proof of principle in rat sciatic nerve *J. Neural Eng.* **15** 056025
- [48] Neto J P, Baião P, Lopes G, Frazão J, Nogueira J, Fortunato E, Barquinha P and Kampff A R 2018 Does impedance matter when recording spikes with polytrodes? *Frontiers Neurosci.* **12** 1–9
- [49] Zhao Z, Gong R, Zheng L and Wang J 2016 *In vivo* neural recording and electrochemical performance of microelectrode arrays modified by rough-surfaced AuPt alloy nanoparticles with nanoporosity *Sensors* **16** 1851
- [50] Baudrant A and Sacilotti M 1982 The LPCVD polysilicon phosphorus doped *in situ* as an industrial process *J. Electrochem. Soc.* **129** 1109–16
- [51] PI-2600 Series—Low Stress Applications *HD Microsystems* 2009 (www.dupont.com/content/dam/dupont/products-and-services/electronic-and-electrical-materials/semiconductor-fabrication-and-packaging-materials/documents/PI-2600_ProcessGuide.pdf) (Accessed: 03 August 2019)